On the *in-situ* determination of the effective secondary electron emission coefficient in low pressure capacitively coupled radio frequency discharges based on the electrical asymmetry effect

Ranna Masheyeva[1,2,*] ⓘ**, Peter Hartmann**[1] ⓘ**, Lan-Yue Luo**[3]**,**
Karlygash Dzhumagulova[2,4] ⓘ**, Yong-Xin Liu**[5] ⓘ**, Julian Schulze**[6] ⓘ **and Zoltán Donkó**[1] ⓘ

[1] Institute for Solid State Physics and Optics, HUN-REN Wigner Research Centre for Physics, 1121 Budapest, Hungary
[2] Department of General Physics, Satbayev University, 050013 Almaty, Kazakhstan
[3] Department of Engineering Physics, Tsinghua University, 100084 Beijing, People's Republic of China
[4] Research Institute of Experimental and Theoretical Physics, Al-Farabi Kazakh National University, 050040 Almaty, Kazakhstan
[5] Key Laboratory of Materials Modification by Laser, Ion, and Electron Beams (Ministry of Education), School of Physics, Dalian University 1cityof Technology, Dalian 116024, People's Republic of China
[6] Chair of Applied Electrodynamics and Plasma Technology, Faculty of Electrical Engineering and Information Sciences, Ruhr University Bochum, 44801 Bochum, Germany

E-mail: masheyeva.ranna@gmail.com

CrossMark

Abstract

We present a method for the *in-situ* determination of the effective secondary electron emission coefficient (SEEC, γ) in a capacitively coupled plasma (CCP) source based on the γ-dependence of the DC self-bias voltage that develops over the plasma due to the electrical asymmetry effect (EAE). The EAE is established via the simultaneous application of two consecutive radio-frequency harmonics (with a varied phase angle) for the excitation of the discharge. Following the measurement of the DC self-bias voltage experimentally, particle-in-cell/Monte Carlo collision simulations coupled with a diffusion-reaction-radiation code to compute the argon atomic excited level dynamics are conducted with a sequence of SEEC values. The actual γ for the given discharge operating conditions is found by searching for the best match between the experimental and computed values of the DC self-bias voltage. The $\gamma \approx 0.07$ values obtained this way are in agreement with typical literature data for the working gas of argon and the electrode material of stainless steel in the CCP source.

---

* Author to whom any correspondence should be addressed.

J. Phys. D: Appl. Phys. **58** (2025) 045208

R Masheyeva *et al*

The method can be applied for a wider range of conditions, as well as for different electrode materials and gases to reveal the effective SEEC for various physical settings and discharge operating conditions.

Keywords: capacitively coupled plasma, particle in cell simulation, secondary electron yield

1. Introduction

Capacitively coupled plasmas (CCPs) driven by radio frequency (RF) waveforms have a wide range of applications for surface modification, layer deposition and etching, in, e.g. microelectronics [1–3]. Since the RF current can flow through dielectric substances as well, the processing of non-conducting samples is also possible, significantly expanding the range of applications. High-energy ion bombardment can improve etching anisotropy, which is useful for deep silicon etching of memory chips, while gentle bombardment with low-energy ions helps improve the etching selectivity, which has been widely adopted in atomic layer etching and deposition processes. Other properties of the surfaces (e.g. wettability) can also be changed by plasma processing. However, the surrounding surfaces (including the electrode surfaces) can also alter the characteristics of the plasma via particle reflection, absorption and generation, which processes are characterized by 'surface coefficients'.

To reveal the fundamentals of RF CCPs and to achieve their most effective utilisation in processing applications, knowledge-based optimization of these plasma sources is necessary [4–8], which requires well-defined laboratory experiments and reliable numerical simulations. The latter also provide access to plasma parameters that are impossible or difficult to measure in experiments. Moreover, validated computational simulations can be used for the plasma source design and process development saving significant time and costs.

Simulations require a set of input data, which describe the interaction of the charged species and radicals with the background gas as well with the surfaces that surround the plasma [9–16]. Among these data, the ones that describe the interaction of the plasma species with the surrounding surfaces are often not known with the desired accuracy [17]. From the plasma, several types of species can reach the electrode surfaces. These include ions, electrons, metastable and fast neutrals, as well as photons. Concerning the ions, under steady-state operation of CCPs only positively charged species can cross the sheaths and negative ions are usually confined within the plasma bulk. These positive ions can cause the emission of secondary electrons from the electrodes. Metastable species, fast neutrals (originating from ion-neutral collisions), and short-wavelength photons can likewise cause secondary electron emission. The efficiency and the contribution of these species varies largely with surface materials and operating conditions. Fairly complete information about these processes is available only for few cases, e.g. for low-current DC (Townsend) discharges in argon [9]. At high-enough energies, ions and neutrals can also cause the sputtering of the

electrodes [18]. Moreover, electrons reaching the surfaces from the plasma can be elastically or inelastically reflected, or can induce the emission of additional electrons [19].

From the manifold of these effects only a subset is usually considered in the numerical characterisations of CCPs. This is indeed a reasonable approximation as long as the pressure is not 'too low' and the discharge voltage is not 'too high'. In the range of pressures between a few times 10 Pa and few times 100 Pa, and at voltages in the range of a few times 100 V, the mean energy of the ions remains below the threshold for kinetic contribution to the ejection of secondary electrons. Under these conditions, no sputtering of the electrode material takes place either. Regarding incoming electrons, which have a low mean energy as well at the above conditions, only elastic reflection is expected to occur, which can be characterised by an elastic reflection coefficient, R. Also, ion-neutral collisions are not expected to create fast neutrals, so their contribution to the emission of secondary electrons can be ignored. The remaining mechanisms, i.e. secondary electron emission due to positive ions (via the potential ejection mechanism), metastable particles, and photons is usually considered via an effective secondary electron emission coefficient SEEC, γ.

In many cases, even these coefficients are not available to modelers for various gas/electrode material combinations due to the unknown effects of the plasma on the surface and a lack of *in-situ* surface diagnostics, despite the fact that these can change plasma characteristics [20, 21], the chemistry in the plasma [22], influence the separate control of ion properties in dual-frequency discharges [23], and can create plasma asymmetry when the surface coefficients differ at the two electrodes [24, 25]. The situation is further complicated by the fact that these values depend on the electrode surface conditions, which are influenced by the actual operating conditions of the discharge. Furthermore, the surface coefficient values available in the literature often originate from surface physics experiments conducted under ultra-high vacuum conditions with heavily sputtered samples, which scenario differs strongly from those found in practical discharge physics experiments and applications [9].

Therefore, during the past years a number of studies applying various approaches have been carried out to determine the values of γ and R, *in situ*. These studies have all combined experimental recordings of some plasma characteristics and computational studies in which the same characteristics have been derived as a function of the surface coefficients. The determination of the latter was based on finding the best agreement between the measured and computed data.

One of the works, presenting an optical method called 'γ-CAST' [26], has focused on a CCP operated in argon gas. The

method was based on the measurement of the spatio-temporal distribution of the excitation rate of an atomic transition with high threshold energy. In such an 'excitation map', the most common feature is the so-called 'α-peak' that originates from the energy gain of the electrons in the vicinity of the expanding sheaths [27]. Secondary electrons emitted from the electrodes and accelerated by the sheath electric field can give rise to another excitation pattern, the so-called 'γ-peak' that appears in the vicinity of the edge of the fully expanded sheaths. In this approach, to determine the effective γ, the intensity ratio of the α- and γ-peaks, derived from phase resolved optical emission spectroscopy (PROES) measurements was compared to that obtained from particle-in-cell/Monte Carlo collisions (PIC/MCC) simulations conducted at the same discharge conditions.

In [28], various diagnostic methods including PROES to measure the spatio-temporally resolved electron impact excitation dynamics, Langmuir probe measurements to quantify the plasma density in the center of the reactor, as well as retarding field energy analyzer measurements to obtain the ion flux-energy distribution at the grounded electrode were used in conjunction with PIC/MCC simulations for finding the *in-situ* values of γ and R by a systematic variation of pressure and voltage.

Precise energy-resolved mass spectrometry measurements of the ion flux-energy distribution function (IEDF) were used in [29] to determine the same pair of surface coefficients in an argon CCP with stainless steel and aluminum oxide electrode surfaces. The study was based on the comparison of the measured and computed IEDFs, with focus on the bimodal peak structure of the IEDF, which is caused by ions crossing the sheath without collisions.

In a recent paper [30], we have proposed an alternative way to determine the surface coefficients discussed above, via the measurement of the DC self-bias voltage, η, that develops in a geometrically symmetrical CCP due to the electrical asymmetry effect [4] when a multi-frequency waveform

$$\phi_0(t) = \sum_{k=1}^{N_H} \phi_k \cos\left(k2\pi f_1 t + \theta_k\right), \quad (1)$$

is supplied by the generator to the plasma. Due to the electrical asymmetry effect (EAE), the voltage drop over the plasma becomes

$$\phi(t) = \phi_0(t) + \eta. \quad (2)$$

here, N_H is the number of harmonics, f_1 the 'base' RF, ϕ_k and θ_k, respectively, the amplitude and the phase of the kth harmonic. In [30], a dependence of η on the SEEC was identified, together with a marginal sensitivity on the elastic electron reflection coefficient. These dependencies led us to conclude that the method is not easily applicable for the determination of R, but has a good prospect for the measurement of γ in CCPs *in situ* via the measurement of the DC self-bias voltage. Here, we demonstrate the application of this method for the

measurement of the SEEC in an Ar CCP operated with stainless steel electrodes.

Following this introduction, the experimental setup and the basics of the computational method will be described in sections 2 and 3, respectively. Section 4 is devoted to the presentation and the discussion of the results. A brief summary is given in section 5.

2. Experiments

In the experiments, our aim is to measure the DC self-bias voltage generated in a geometrically symmetric CCP source operated with EAE excitation, realised by a waveform defined by equation (1) [31]. The operating conditions in the experiment have to be chosen carefully, in a way that (i) a precise measurement of the RF discharge voltage waveform is possible and (ii) the secondary electron emission from the electrodes has a strong effect on the measured DC self-bias voltage. The conditions to be chosen include the base frequency (f_1) and the number of harmonics (N_H) in the excitation waveform (equation (1)), as well as the voltage amplitudes (V_k) of these harmonics, and the gas pressure (p). The selection of these parameters is discussed below together with the description of the experimental apparatus.

Based on our prior computational studies [30] we estimate that an accuracy of a few Volts of the RF voltage measurement in the experiment is required for the determination of the γ coefficient. This requirement translates to about (a non-trivial) few percent accuracy considering the fact that RF excitation voltages are typically in the 100 V range. Such accurate measurements are increasingly difficult at higher frequencies due to the wave nature of the excitation signal and its complicated interaction with the plasma source. CCP cells usually have resonances similar to dipole antennas and whenever the operating frequencies are not far enough from these resonances, the gap (discharge) voltage may become significantly different from that measured at the external contact points [32]. While in principle one can model the plasma source with a discrete equivalent electrical circuit [33], the best solution is to keep the operating frequency and the resonances of the source far from each other.

As a preparation for the experiments, we determined the frequency response of our standard experimental CCP cell (Budapest V3 CCP [34]), by measuring its S_{11} complex reflection parameter using a vector network analyzer (type PicoVNA 106) in a 1-port mode. In this measurement, the frequency was scanned between 1 MHz and 100 MHz and as figure 1(a) shows, a large resonance was found to be present at about 70 MHz. This is also clearly seen in panel (b) of this figure, which displays the complex impedance derived from the S_{11} parameter. This finding motivated us to construct a smaller and much simplified CCP cell, the 'XS Cell'. This cell consists of a glass cylinder with an inner diameter of 92 mm and a pair of stainless steel electrode plates facing each other at a distance of $L = 27.5$ mm, as shown in figure 2. The VNA measurement was repeated on this cell over a frequency range
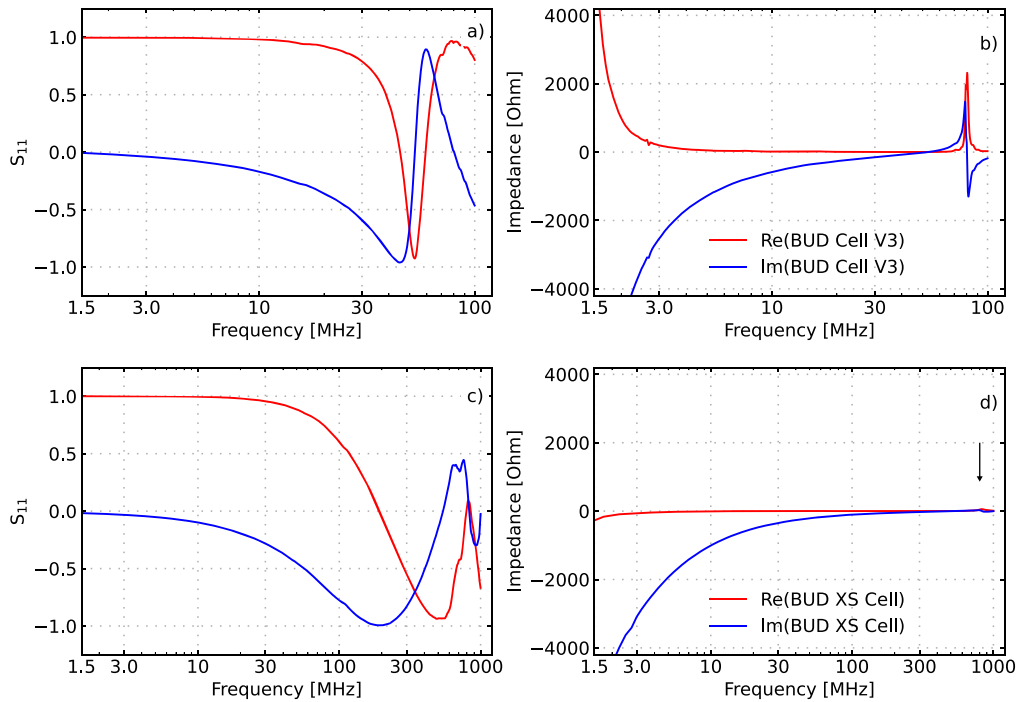
Figure 1. Complex reflection parameter, S_{11} (a) and complex impedance (b) of the 'BUD Cell V3' and the same quantities for the 'BUD XS Cell' (c), (d) cell built for the present measurements. 'Re' and 'Im' mark the real and imaginary parts of the respective quantities, the arrow in (d) points to the weak resonance of the XS cell around 800 MHz.
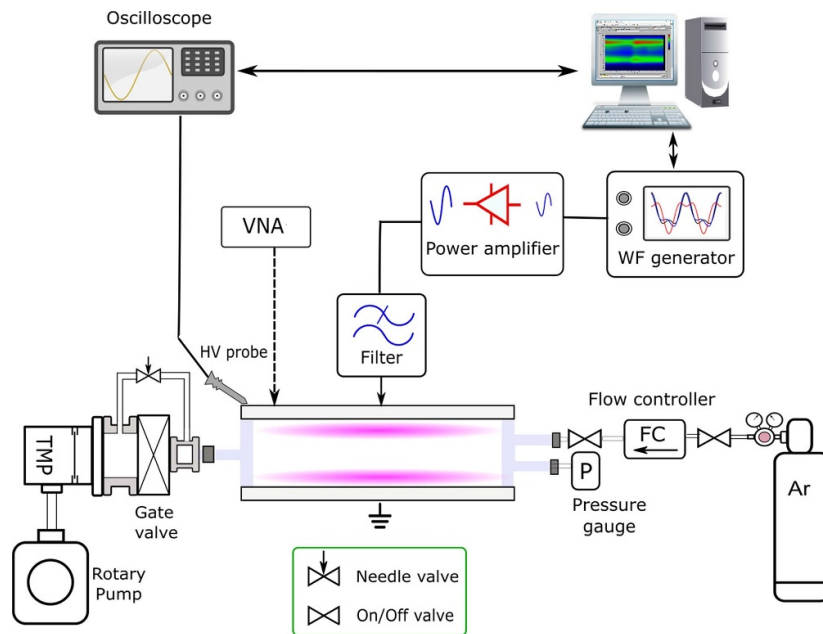

Figure 2. Experimental setup including the vacuum and gas filling system and the electronics / control systems.

of 1 MHz−1000 MHz. The frequency response showed a resonance at a much higher frequency (see figure 1(d)), making this cell more appropriate for our measurements.

To optimise the effect of the secondary electron emission on the discharge characteristics, including the DC self-bias, a lower-frequency operation of the system (as compared to the usual base frequency of 13.56 MHz) is preferred as electron 'heating' by sheath expansion is reduced at lower excitation frequency. To limit the range of operation frequencies, the number of harmonics in the excitation waveform, N_{H}, has to be limited, too. While a higher number of harmonics results in a higher value of the DC self-bias [30, 35], which would be favorable for our measurements, increasing N_{H} creates technical difficulties. Considering the above arguments,
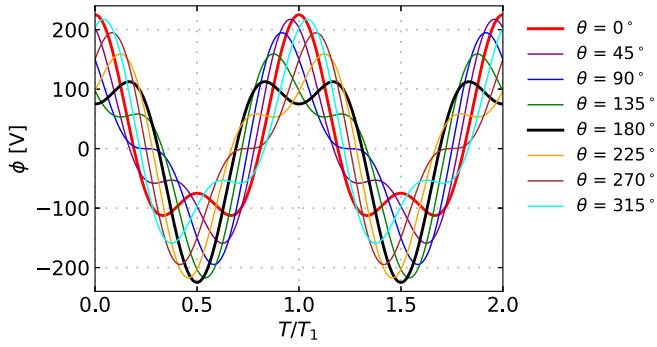
Figure 3. Driving voltage waveform examples for two low frequency periods ($T_1 = 1/f_1$), at $\phi_1 = 150$ V and $\phi_2 = 75$ V. Peaks- and valleys-waveforms are realised by selecting $\theta = 0°$ and $180°$, respectively.

our choice is to select $N_H = 2$, i.e. we use the generator waveform

$$\phi_0(t) = \phi_1 \cos(2\pi f_1 t) + \phi_2 \cos(4\pi f_1 t + \theta), \qquad (3)$$

with base frequency values of $f_1 = 2$ MHz and 4 MHz.

Earlier studies of the EAE have found that the DC self bias can be maximised by setting the relative amplitudes of the harmonics in the driving voltage waveform according to a specific relation given in [35]. For $N_H = 2$, the optimum voltage amplitudes are related as $\phi_2 = 0.5 \phi_1$. In the experiments, we have thus selected $\phi_1 = 150$ V and $\phi_2 = 75$ V for both $f_1 = 2$ MHz and $f_1 = 4$ MHz base frequencies. Figure 3 shows examples of the driving voltage waveforms at selected values of θ.

The phase-locked harmonics composing the waveform defined by equation (3) are generated by a two-channel RF signal generator (Multicomp pro MP750389). This generator allows setting the phase angles and the amplitudes of the two harmonics separately. The waveform is fed to a broadband amplifier (Vectawave VBA100-200) and is applied to the top electrode of the XS cell via a filter that suppresses eventual higher harmonics, see figure 2. No matching circuit is applied, but at the low power levels used, the reflected power does not represent an issue for the amplifier and in the experiments the optimisation of the applied waveform is the main goal and not the optimisation of power coupling. The actual waveform at the powered electrode (which may differ from the waveform generated by the signal generator, both in terms of the phase between the harmonics and the ratio of their amplitudes) is measured by a Tektronix MSO44 oscilloscope equipped by a high-voltage probe, type Tektronix P5100A. The oscilloscope is connected to a computer that runs a Labview code, which provides feedback [36] to the signal generator to correct the phases and the voltage amplitudes in a way that the desired waveform is present at the powered electrode. As even with this feedback loop there are small differences between the measured waveform and the theoretical waveform given by equation (3), the measured waveforms are stored and are applied subsequently in the simulations instead of the theoretical waveforms.

By applying a voltage waveform given by equation (3), the DC self-bias is controlled by the phase angle θ. By scanning

θ over the $[0, 2\pi]$ interval the $\eta(\theta)$ function exhibits a nearly triangular shape with relatively flat parts near the maximum and minimum [31] (see below in figure 4). Although the oscilloscope, which records the RF voltage, has a wide frequency bandwidth, the connecting cable introduces a finite time delay, τ, on the order of a few nanoseconds. As this time delay influences the phases of both measured RF voltage components, it leads to a measured phase, θ^*, being somewhat different from θ. Running the experiments at the relatively low base frequencies selected ensures that $\tau \ll (T_1 = 1/f_1, T_2 = 1/2/f_1)$. Nonetheless, even at such conditions, it is preferred to carry out measurements at a phase angle where the $\eta(\theta)$ function is (relatively) flat. This is met in the vicinity of the extrema of the $\eta(\theta)$ functions, i.e. at/near $\theta = 0$ and 180 degrees. Therefore the match between the measured and computed bias voltage values is searched for at these phase angles.

Finally, the choice of the gas pressure is motivated by the following arguments. At low pressures, where the electron kinetics is highly non-local, the secondary electrons emitted from the electrodes deposit their energy (gained within the sheaths adjacent to the electrodes) over the entire electrode gap. At higher pressures, the electron kinetics has a more local character and the secondary electrons are expected to influence more strongly the ionization in the regions adjacent to the electrodes from which these were emitted. Consequently, we expect a larger effect of the secondary electron emission on η at higher pressures. At the given electrode gap, therefore, we choose operating pressures of $p = 40$ Pa and 80 Pa for our measurements. Using higher pressures would also require extension of the discharge model with additional species (see also in section 3).

The gas pressure is measured by a capacitive gauge of type Pfeiffer Vacuum CMR363 and the experiments are conducted in a steady (2.8 sccm) flow of the Ar gas (of purity 6.0) established by a flow controller (type GFC17A-VAL6-A0).

At the conditions selected, the power absorbed by the plasma is relatively low and the increase of the temperature of the gas is expected to be insignificant.

3. Computational method

At the gas pressures of interest here, the populations of Ar atoms in the excited levels become important, especially in the metastable ($1s_5$ and $1s_3$ (in Paschen notation)) and the resonant ($1s_4$ and $1s_2$) levels [37–39]. Thus, we use the computational approach that we developed in [39], which consists of a PIC/MCC module and a Diffusion-Reaction-Radiation (DRR) module. The PIC/MCC code traces electrons and Ar^+ ions (more precisely electron and ion 'superparticles') in the neutral background gas that comprises ground-state Ar atoms and Ar atoms in 30 excited levels [40]. Molecular ions, which may become important at higher pressures [41] are not considered in the present model.

The DRR module computes the spatial density distributions of the Ar atoms in these excited levels, based on the rates of the electron-impact collision processes obtained in the PIC/MCC module and the rates of the radiative channels (spontaneous

emission and re-absorption) within the system of the excited levels and between some of these excited levels and the Ar atom ground-state. The calculations also take into account pooling ionization between the excited atoms, electron-impact stepwise ionization from the excited levels, quenching of the excited levels by neutrals, as well as diffusion losses. The volume and surface processes included in the discharge model and discussed below in some detail, are listed in table 1.

The PIC/MCC simulation considers a one-dimensional spatial geometry: the plasma forms between two plane and parallel electrodes; one of these, situated at $x = 0$ is powered by a waveform similar to equation (3), but is taken from experimental recordings for enhanced precision (see section 2). The other electrode at $x = L$, is grounded. The particles' motion is followed in the three-dimensional velocity space. The approach uses the electrostatic approximation [52] and adopts an equidistant numerical grid with $N_g = 512$ points and a resolution of Δx, for the calculation of the electric potential and the densities of the charged species. These quantities are computed at discrete values of the time, separated by $\Delta t = T/N_t$ where N_t is the number of time steps within a base RF period $T = 1/f_1$. Depending of the pressure and the base frequency (f_1), we use $N_t = 18\,000\ldots72\,000$ time steps to ensure that the probability of the collisions of the charged species during one time step is kept at a low value ($<5\%$). Poisson's equation is solved for the electric potential by taking the electrode potentials as boundary conditions and including the space charge created by the particles, using the Thomas algorithm. The equation of motion of the charged particles is integrated using the leapfrog scheme. While electrons are advanced at each time step, Ar^+ ions are advanced only in every 20th time step ('ion subcycling'), i.e. $\Delta t_i = 20\Delta t_e$. These simulation settings fulfil the stability and accuracy criteria of the PIC/MCC scheme (see, e.g. [53, 54]).

The charged-neutral particle collisions are treated with a Monte Carlo approach (e.g. [55]), the probability of a collision of type j being:

$$P_{\text{coll},j} = 1 - \exp\left[-n_{\text{target}}(x)\,\sigma_j(\varepsilon)\,g\Delta t\right], \qquad (4)$$

where ε is the center-of-mass energy of the colliding particles, $n_{\text{target}}(x)$ is the density of the target species at the spatial location x where P_{coll} is computed, σ_j is the cross section of process j, $\varepsilon = \mu g^2/2$ with μ being the reduced mass of the collision partners (the projectile and the target) and $g = |\mathbf{v}_{\text{proj}} - \mathbf{v}_{\text{target}}|$ the relative velocity between these. In case of ion projectiles, $\mathbf{v}_{\text{target}}$ is sampled from the thermal distribution of the background gas atoms, while in the case of electrons $\mathbf{v}_{\text{target}}$ is set to zero, i.e. in this case we use the 'cold gas approximation'. The density of the target atoms is constant for the ground-state Ar atoms, $n_{\text{target}}(x) = n_g$, while it has a space-dependence in case of Ar atoms in the excited levels. The set of collision processes between electrons and ground-state Ar atoms includes elastic scattering, excitation to 30 specific Ar-I levels and a lumped 'Rydberg' level, as well as ionization, with cross sections taken from the BSR database [42] of LxCat [56, 57]. The cross sections of stepwise excitation processes are taken

from [40, 42], the cross sections for the electron-impact de-excitation processes are derived from these using the principle of detailed balance [58]. In this work, we use a subset of the processes as compared to the full set used in [39] to increase the computational speed. The actual list of electron-impact processes is provided in the appendix.

The cross section for the stepwise electron-impact ionization from the 1s levels is adopted from [43], stepwise ionization from the 2p levels is not considered here based on the studies reported in [59]. The rate of pooling ionization processes is taken from [44]. For the Ar^+ ions, we use the approach of [45], and take into account (elastic) backscattering and isotropic scattering processes.

The interaction of the charged particles with the boundary surfaces includes (i) the elastic reflection of the impinging electrons, characterised by the coefficient R and (ii) the neutralisation of the ions and, associated with this, the emission of secondary electrons with a probability expressed by the (effective) SEEC, γ. Based on earlier studies [28, 29] we adopt the value of $R = 0.7$. This simplified approach is justified by the low energy of the electrons that reach the electrodes at times of sheath collapse (see section 1). For the ion-induced electron yield, γ, various values are used at otherwise fixed discharge conditions, in order to find the actual value of this coefficient under the given discharge conditions, by comparing the experimentally measured and the computed values of the DC self-bias voltage. As explained in section 1, γ is an effective value that accounts implicitly for the contributions of other species [9] that contribute to secondary electron emission.

The DC self-bias voltage, η, is determined in an iterative manner in the simulations. At the initialization of the simulation, $\eta = 0$ V is set. After executing the simulation for a given number of RF cycles, the time-averaged currents of the electrons and Ar^+ ions are compared at each electrode. Depending on the balance of these currents, the DC self-bias voltage is adjusted by a small quantity. This procedure is continued until η reaches a converged value and the time-averaged charged particle currents balance each other in the PIC/MCC simulation at any of the electrodes.

The DRR part of the model makes use of the spatially-resolved rates of the electron-impact collision processes (obtained in the PIC/MCC simulation) to derive the spatial density distributions of the Ar atoms in the various excited levels via solving the diffusion equations of these species (see [39]). These equations also include terms for the pooling ionization processes, quenching of the excited atoms by collisions with neutrals, as well as radiative transitions. For the sources of data relevant to these processes, see table 1. The diffusion equations are solved using an explicit, finite difference forward-time-centered-space method [37, 60]. For more details, see [59]. The low flow velocity of the gas in the experimental cell is not included in the simulations.

As revealed in [59], the transitions between the Ar 2p and 1s levels are partly trapped, and thus the reabsorption of the radiation has to be considered for these transitions as well, besides the heavily trapped resonant lines. This effect is incorporated

Table 1. Elementary processes considered in the model in the plasma volume and at the surfaces. Ar* and Ar** denote excited levels, $\varepsilon(\text{Ar}^*) < \varepsilon(\text{Ar}^{**})$. Ar^r and Ar^m denote the lowest resonant (1s$_4$ and 1s$_2$) and the metastable (1s$_5$ and 1s$_3$) levels. GS: ground state. In the case of radiative processes, '$\times 2$' indicates that both spontaneous emission and re-absorption processes are taken into account. A detailed list of the electron-impact processes is given in the appendix

Reaction	Name	# Of proc.	Reference
$e^- + \text{Ar} \rightarrow e^- + \text{Ar}$	elastic scattering	1	[42]
$e^- + \text{Ar} \rightarrow e^- + \text{Ar}^*$	direct excitation	31	[42]
$e^- + \text{Ar} \rightarrow 2e^- + \text{Ar}^+$	direct ionization	1	[42]
$e^- + \text{Ar}^* \rightarrow e^- + \text{Ar}^{**}$	stepwise excitation & de-excitation	69	[42]
$e^- + \text{Ar}^* \rightarrow 2e^- + \text{Ar}^+$	stepwise ionization	4	[43]
$\text{Ar}^{r,m} + \text{Ar}^{r,m} \rightarrow e^- + \text{Ar}^+ + \text{Ar}$	pooling ionization	10	[44]
$\text{Ar}^+ + \text{Ar} \rightarrow \text{Ar}^+ + \text{Ar}$	elastic scattering (isotropic & backward)	2	[45]
$\text{Ar}^* \leftrightarrow \text{Ar} + \text{photon}$	spont. em. & re-abs. to/from GS	7×2	[46]
$\text{Ar}^{**} \leftrightarrow \text{Ar}^* + \text{photon}$	spont. em. & re-abs. between exc. levels	136×2	[46]
$\text{Ar}^m + (2)\text{Ar} \rightarrow \text{Ar} + (2)\text{Ar}$	2- & 3-body quenching by neutrals	4	[47]
$\text{Ar}^* + \text{Ar} \rightarrow \text{Ar} + \text{Ar}$	2-body quenching of 2p levels by neutrals	10	[48, 49]
$\text{Ar}^* + \text{wall} \rightarrow \text{Ar} + \text{wall}$	diffusion to boundaries	30	[50, 51]
$\text{Ar}^+ + \text{wall} \rightarrow \text{Ar} + \text{wall} + e^-$	neutralization & secondary e$^-$ emission	1	
$e^- + \text{wall} \rightarrow e^- + \text{wall}$	elastic electron reflection	1	[28]

into the model by adopting an escape factor appropriate for a slab geometry. We use the data from [61] and [62]. (As in [59], we use equations (6a) and (6b) of [62], which originate from [61], but in [62] typographical errors of these equations in [61] have been corrected.)

The PIC/MCC and the DRR modules are executed in an iterative loop until the converged solution at a given set of discharge conditions is obtained. Convergence is monitored in terms of the number of superparticles, the densities of the excited atoms in the various levels, as well as the DC self-bias voltage. Convergence is typically reached after running the simulation for several thousands of RF cycles.

The simulation code has previously been benchmarked with experimental data for spatially resolved metastable atom density distributions [39] and for optical emission line intensities of the plasma [59].

4. Results and discussion

The measurements and the simulations are carried out for Ar gas at pressures of $p = 40$ Pa and 80 Pa, for base frequency values of $f_1 = 2$ MHz and 4 MHz, voltage amplitudes $\phi_1 = 150$ V and $\phi_2 = 75$ V, and for an electrode gap of $L = 2.75$ cm. In the computations, we use a range of effective secondary electron yield values, $0 \leqslant \gamma \leqslant 0.2$. As it was already mentioned above, due to slight differences between the measured waveform and the theoretical waveform the measured waveforms are applied to the powered electrode in the simulations.

The collection of the four sets of experimental results for the dependence of the DC self-bias voltage, η, on the phase angle, θ, are shown in figure 4 as solid lines. It is noted that although the CCP cell is geometrically symmetric, a small DC self-bias voltage of -13 V $\leqslant \eta_0 \leqslant -9$ V, depending on the discharge conditions, is generated by the asymmetry of the power and grounding connections even when the discharge is driven
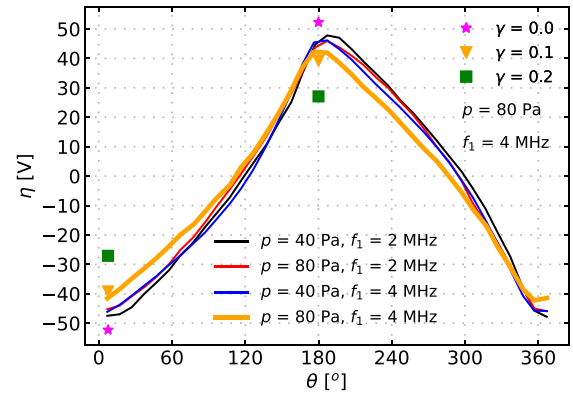
Figure 4. Experimentally measured DC self-bias voltage as a function of the phase angle θ (solid lines) for $p = 40$ Pa and 80 Pa, $f_1 = 2$ MHz and 4 MHz (and $L = 2.75$ cm, $\phi_1 = 150$ V, $\phi_2 = 75$ V. The discrete data points show the computed DC self-bias voltages at $\theta = 0°$ and $180°$ for $p = 80$ Pa and $f_1 = 4$ MHz, for γ values of 0, 0.1, and 0.2.

by a single harmonic waveform. These self-bias values are subtracted from the η values measured under dual-frequency excitation, i.e. $\langle \eta(\theta) \rangle_\theta = 0$ V is ensured for all the curves presented in figure 4.

The nearly 'triangular' shape of the $\eta(\theta)$ curves matches well the previous experimental and simulation results [31]. For the extrema of the bias voltage we find $|\eta| \approx 42 - 47$ V, depending on the discharge conditions. These extrema occur near, but not exactly at $\theta = 0°$ and $180°$, i.e. when peaks- and valleys-type waveforms are imposed by equation (3), see also figure 3. This small angular shift is due to the charge dynamics in the CCP [63]. At $\theta = 0°$ and $\theta = 180°$, figure 4 also shows the DC self-bias voltage values obtained from the PIC/MCC simulations at $p = 80$ Pa, $f_1 = 4$ MHz, for γ values of 0, 0.1, and 0.2. These data points indicate that (i) the magnitude of
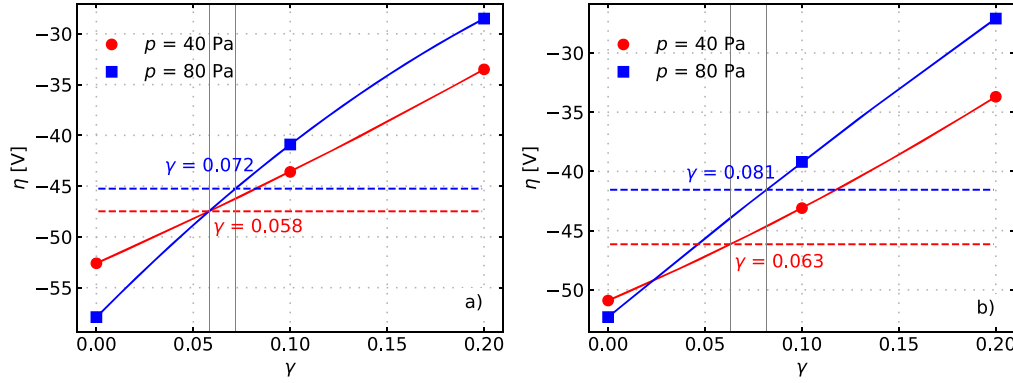
Figure 5. Computed DC self-bias voltage at $\theta = 0°$ as a function of γ (solid lines with symbols). Discharge conditions: Ar, $p = 40$ and 80 Pa, $f_1 = 2$ MHz (a) and 4 MHz (b), $\phi_1 = 150$ V, $\phi_2 = 75$ V, $L = 2.75$ cm. The dashed horizontal lines correspond to the experimental data (red: 40 Pa, blue: 80 Pa) for the DC self-bias. The solid lines are parabolic fits to the computed η values.

Table 2. Measured DC self-bias voltage η and the effective SEEC γ for the various discharge conditions.

f_1	p	η	γ
2 MHz	40 Pa	-47.5 V	0.058
4 MHz	40 Pa	-46.2 V	0.063
2 MHz	80 Pa	-45.3 V	0.072
4 MHz	80 Pa	-41.6 V	0.081

Figure 6. Measured and computed $\eta(\theta)$ curves for $\gamma = 0.07$. Discharge conditions: Ar, $p = 80$ Pa, $L = 2.75$ cm, $f_1 = 4$ MHz, $\phi_1 = 150$ V, $\phi_2 = 75$ V, $R = 0.7$.

the self-bias voltage decreases with increasing γ in agreement with the findings of [30] and that (ii) the effective secondary electron yield is in the $0 \leqslant \gamma \leqslant 0.1$ domain for the $p = 80$ Pa and $f_1 = 4$ MHz parameter combination.

Figure 5 illustrates the dependence of the computed DC self-bias voltage on γ for the two values of the base frequency, $f_1 = 2$ MHz (a) and $f_1 = 4$ MHz (b), at pressures of 40 Pa and 80 Pa. The experimental self-bias voltage values for the respective cases are represented by the dashed horizontal lines, while the numerical results are shown as symbols. The intersections of the latter and the horizontal lines identify the corresponding γ values, which are marked by thin gray vertical lines. The corresponding numerical values are given in table 2. For the conditions covered here, we find $\gamma = 0.07 \pm 0.012$, which is in good agreement with the findings of previous studies, including the determination of the SEEC by matching simulation results with (i) experimentally measured ion energy distribution functions [29] and (ii) the spatio-temporal distributions of the electron-impact excitation rate (obtained experimentally by PROES) [28]. It is also noted that this γ value is near the SEEC given in [9] for low-energy Ar$^+$ ions on metal surfaces.

Figure 6 compares the measured DC self-bias voltage with the computed one over the whole domain of the phase angle θ for the $\gamma = 0.07$ value at $p = 80$ Pa and $f_1 = 4$ MHz. The measured and computed curves exhibit a very good agreement (concerning the shape of the whole curve as well, in addition to the matching values at the extrema), confirming the consistency of
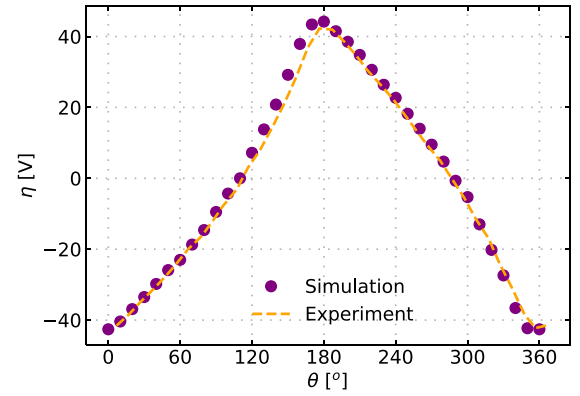
the model and the correctness of the effective secondary electron yield of approximately 0.07.

In order to reveal the physical reasons of the dependence of the DC self-bias voltage on the SEEC we invoke the analytical model of the EAE [64] in the forthcoming analysis. According to this model, the DC self-bias is given by

$$\eta = -\frac{\phi_{\max} + \varepsilon\phi_{\min}}{1 + \varepsilon} + \frac{\phi_{\mathrm{sp}}^{\mathrm{f}} + \varepsilon\phi_{\mathrm{sg}}^{\mathrm{f}}}{1 + \varepsilon} + \frac{\phi_{\max}^{\mathrm{b}} + \varepsilon\phi_{\min}^{\mathrm{b}}}{1 + \varepsilon}, \quad (5)$$

where $\phi_{\max}$ and $\phi_{\min}$ are the maximum and minimum of the applied RF voltage waveform, $\phi_{\mathrm{sp}}^{\mathrm{f}}$ and $\phi_{\mathrm{sg}}^{\mathrm{f}}$ are the floating potentials at the powered and grounded electrodes (the minimum voltage drops across the respective sheath within each period of the fundamental driving frequency), $\phi_{\max}^{\mathrm{b}}$ and $\phi_{\min}^{\mathrm{b}}$ are the voltage drops across the plasma bulk at the times of maximum and minimum applied voltage, respectively. Moreover, ε is the symmetry parameter, which is the ratio of the peak values of the sheath voltages at both sides of the plasma:
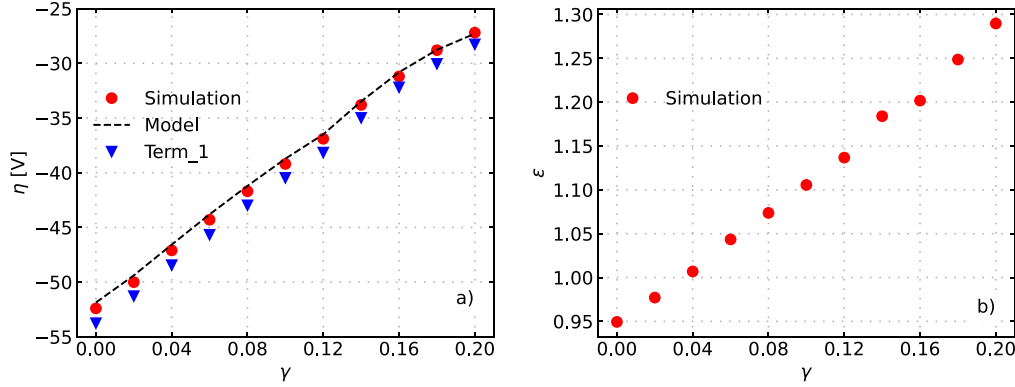
Figure 7. (a) Dependence of the computed DC self-bias voltage on γ, for $p = 80$ Pa, $L = 2.75$ cm, $f_1 = 4$ MHz, $\phi_1 = 150$ V, $\phi_2 = 75$ V, $R = 0.7$, at $\theta = 0°$. 'Model' refers to η values computed by equation (5) using PIC/MCC data, while 'Term 1' refers to the first term of the same equation. (b) Dependence of the assymetry parameter on the effective secondary electron yield.

$$\varepsilon = \left| \frac{\widehat{\phi}_{\text{sg}}}{\widehat{\phi}_{\text{sp}}} \right|. \tag{6}$$

All the quantities appearing in the above equations can readily be obtained from the PIC/MCC simulations.

Figure 7(a) compares the DC self-bias voltage computed directly in the simulation and from equation (5) (marked as 'Model', using the PIC/MCC data for the respective quantities) for the $p = 80$ Pa and $f_1 = 4$ MHz case. The figure also shows the value of the first term of equation (5), marked as 'Term 1'. The values of the first term are found to be very close to the sum of the three terms, implying that the contributions of the floating potentials and the bulk voltage drop, i.e. the second and third terms of expression (5) (not shown in figure 7(a)) are small compared to the first terms. The data show that both of these terms acquire a small positive value of about 1 V, regardless of γ. This implies that it is mainly the first term of equation (5) that is responsible for the effect of γ on the DC self-bias voltage. On the other hand, the small effects of the sheath floating potentials and the voltage drop over the plasma bulk also contribute to the effect studied.

Next, we therefore analyze the dependence of ε on γ, based on figure 7(b). As in the expression for η (equation (5)), ϕ_{max} and ϕ_{min} are constant at a fixed phase angle, it can be concluded that the dependence of η on γ is defined by the change of the symmetry parameter as a function of γ. The symmetry parameter exhibits a monotonic increase as a function of γ, which is in turn a consequence of the variation of the peak sheath voltage values on γ.

According to the analytical model of the EAE, the peak sheath voltages can be expressed as:

$$\widehat{\phi}_{\text{sp}} = -\frac{1}{2e\varepsilon_0} \left(\frac{Q_{\text{mp}}}{A_{\text{p}}} \right)^2 \frac{I_{\text{sp}}}{\overline{n}_{\text{sp}}}, \tag{7}$$

and

$$\widehat{\phi}_{\text{sg}} = \frac{1}{2e\varepsilon_0} \left(\frac{Q_{\text{mg}}}{A_{\text{g}}} \right)^2 \frac{I_{\text{sg}}}{\overline{n}_{\text{sg}}}, \tag{8}$$

where e is the elementary charge, ε_0 is the permittivity of free space, $Q_{\text{mp/mg}}$ are the maximum uncompensated charges within the sheaths, $A_{\text{p/g}}$ denotes the electrode surface areas, $I_{\text{sp/sg}}$ the sheath integrals (whose ratio can be approximated by a value of 1 according to [4, 64]), and $\overline{n}_{\text{sp/sg}}$ the mean charged particle densities in the respective sheath. In the symmetric system considered here, $A_{\text{p}} = A_{\text{g}}$. With these, equation (6) becomes

$$\varepsilon = \left(\frac{Q_{\text{mg}}}{Q_{\text{mp}}} \right)^2 \frac{\overline{n}_{\text{sp}}}{\overline{n}_{\text{sg}}}, \tag{9}$$

i.e. understanding of the behavior of η as a function of the secondary electron yield ultimately requires understanding the behaviors of the two terms, $Q_{\text{mg}}/Q_{\text{mp}}$ and $\overline{n}_{\text{sp}}/\overline{n}_{\text{sg}}$, on γ. This analysis is aided by showing spatio-temporal maps of the ionization rate, $S(x,t)$, in figure 8 for a sequence of γ values, as well as by plots of the time-averaged ionization rate, $S(x)$, and the time-dependent total uncompensated charge in the plasma / electrode area, shown in figures 9(a) and (b), respectively. Additional relevant parameters (the DC self-bias voltage, the symmetry parameter, and its relevant terms) are shown in tabulated form in table 3 for various values of γ, at $\theta = 0°$.

At $\gamma = 0$, ionization in the discharge proceeds only via the 'α-mechanism', $S(x,t)$ is high only in the vicinity of the edge of the expanding sheath, see figure 8(a). Due to the specific waveform, the ionization peak at the powered electrode is stronger due to the faster expansion of the powered sheath, as compared to the grounded side of the discharge. As the secondary electron yield grows, a more significant fraction of the ionization occurs within the sheaths, see further panels of figure 8. Because of the peaks-type waveform, the sheath at the powered side is expanded for a long time, compared to the sheath at the grounded side. As a consequence of this, the time-averaged ionization rate grows much more strongly at the powered side of the discharge in response to an increasing γ, as shown in figure 9(a). This explains the growth of $\overline{n}_{\text{sp}}/\overline{n}_{\text{sg}}$ with increasing γ, seen in table 3. We note that the increase of the total ionization rate with increasing γ is due to the increase of the electron-impact ionization rate of ground-state Ar atoms, stepwise ionization and pooling ionization contribute weakly
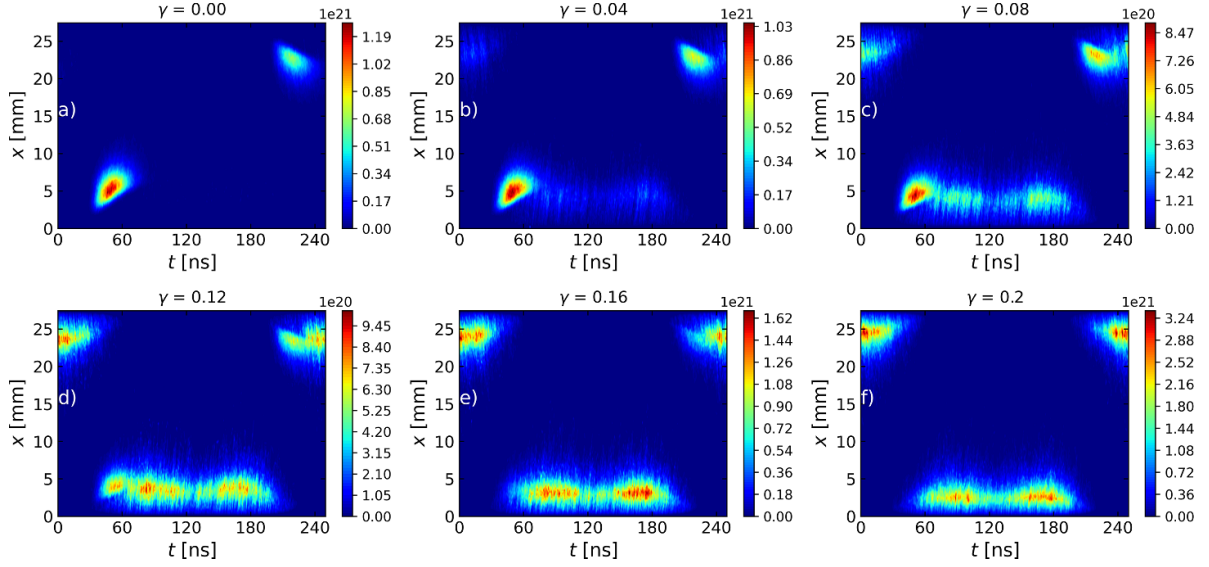
Figure 8. Spatio-temporal distribution of the ionization rate for different values of γ obtained from the PIC/MCC simulations. The powered and grounded electrodes are situated at $x = 0$ mm and 27.5 mm, respectively. Discharge conditions: Ar, $p = 80$ Pa, $L = 2.75$ cm, $f_1 = 4$ MHz, $\phi_1 = 150$ V, $\phi_2 = 75$ V, $R = 0.7$, $\theta = 0°$.
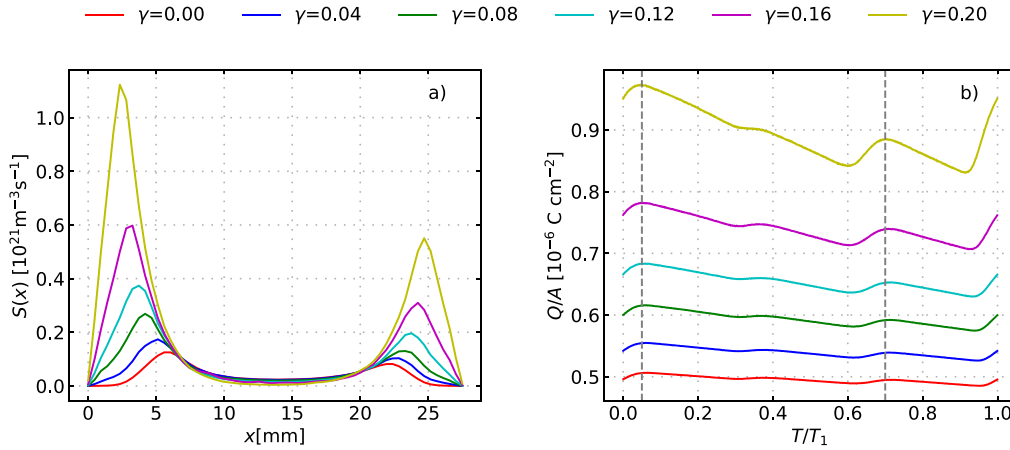

Figure 9. Spatial distribution of the time-averaged ionization rate, $S(x)$, (a) and total uncompensated charge per unit area, Q/A, as a function of time within one fundamental RF period (b) for various values of γ. The vertical lines in panel (b) indicate the times of sheath collapse: $t_p/T_1 \approx 0.05$ marks the sheath collapse at the powered electrode, while $t_g/T_1 \approx 0.7$ marks the sheath collapse at the grounded electrode. Discharge conditions: Ar, $p = 80$ Pa, $L = 2.75$ cm, $f_1 = 4$ MHz, $\phi_1 = 150$ V, $\phi_2 = 75$ V, $R = 0.7$, $\theta = 0°$.

to the total rate at high γ (where their rates are actually smaller as compared to those at low γ, as a consequence of the decreasing metastable atom density with increasing γ).

The behaviour of the other term, $(Q_{mg}/Q_{mp})^2$, relevant for ε (see equation (9)) can be understood by observing the variation of the total uncompensated charge in the plasma, Q, as a function of γ. Figure 9(b) shows this quantity, normalised by the electrode area, A, as a function of time within the fundamental RF cycle. The dynamics of this charge is due to electron and ion currents to the electrodes. Upon sheath collapse, i.e. when electrons are lost from the plasma, Q/A increases. The decrease of Q/A, on the other hand, is due to the continuous losses of ions at the boundary surfaces.

The times of sheath collapses are marked with vertical dashed lines: the first of these, at $t_p/T_1 \approx 0.05$ marks the sheath collapse at the powered electrode, while the second, at $t_g/T_1 \approx 0.7$ the sheath collapse at the grounded electrode. Consequently, at $t = t_p$, the data show Q_{mg}/A and at $t = t_g$, the data show Q_{mp}/A, as the maxima of charges in one sheath appear at times when the other sheath is collapsed. The numerical results in figure 9(b) clearly show that Q_{mg}/Q_{mp} increases with increasing γ, see also the data in table 3. This is a consequence of the increasing ionization rate at the powered side of the plasma, which creates a higher positive ion flux to the powered electrode on time average, as compared to the grounded electrode. To ensure the time-averaged compensation of

Table 3. Self-bias voltage (η) at $\theta = 0°$ as a function of γ, the values of the symmetry parameter ε, and the terms involved in ε, as well as the peak sheath voltages, as obtained from the PIC/MCC results.

γ	$\eta(V)$	$\overline{n}_{\mathrm{sp}}/\overline{n}_{\mathrm{sg}}$	$(Q_{\mathrm{mg}}/Q_{\mathrm{mp}})^2$	ε	$|\widehat{\phi}_{\mathrm{sp}}|(V)$	$\widehat{\phi}_{\mathrm{sg}}(V)$
0.00	−52.4	0.83	1.11	0.95	174	165
0.02	−50.0	0.85	1.10	0.98	171	167
0.04	−47.1	0.88	1.11	1.01	169	170
0.06	−44.3	0.89	1.12	1.04	166	173
0.08	−41.7	0.92	1.12	1.07	163	175
0.10	−39.2	0.94	1.13	1.10	161	178
0.12	−36.9	0.98	1.12	1.14	158	180
0.14	−33.8	0.99	1.14	1.18	155	183
0.16	−31.2	1.04	1.11	1.20	154	185
0.18	−28.8	1.01	1.19	1.25	151	188
0.20	−27.2	1.04	1.20	1.29	148	191

the positive and negative particle fluxes, a higher electron flux is necessary at the powered electrode as well, as compared to that at the grounded electrode. Around times of sheath collapse at the powered side, Q/A indeed grows more significantly than around times of sheath collapse at the powered electrode.

As we found both $\overline{n}_{\mathrm{sp}}/\overline{n}_{\mathrm{sg}}$ and $Q_{\mathrm{mg}}/Q_{\mathrm{mp}}$ to increase with increasing γ, the increase of the symmetry parameter is explained. The increase of ε, in turn, results in a suppression of the DC self-bias voltage as seen in table 3.

Finally, with the aid of the data plotted in figure 7(a) an estimation of the accuracy of our method for the determination of the effective γ can also be given. It is recalled that our experiment involves the measurement of η and the voltage amplitudes ϕ_1 and ϕ_2. As η is a DC quantity, it can be measured highly accurately, as compared to the RF voltage amplitudes (c.f. section 2). For small variations of the voltage amplitudes, the relative DC self-bias, i.e. η/ϕ_1 (or η/ϕ_2), is expected to remain constant [31]. An expected accuracy of the RF voltage amplitude measurement of $\Delta\phi_1 \approx \pm 5$ V translates in $\Delta\eta = (\eta/\phi_1)\Delta\phi_1 \approx 1.25$ V, as in our case $\eta/\phi_1 \approx 1/4$ (at $\gamma \approx 0.07$). The error of γ is therefore $\Delta\gamma = (\mathrm{d}\gamma/\mathrm{d}\eta)\Delta\eta \approx 0.01$, since $\mathrm{d}\eta/\mathrm{d}\gamma$ is about 125 V from figure 7(a). This sensitivity of γ on the RF voltage amplitudes explains why special care had to be taken in the experiments to establish conditions for an accurate determination of the RF voltages. We note that the above numerical data are specific for the $p = 80$ Pa and $f_1 = 4$ MHz case, but for the other conditions covered in this work, similar error values for the γ-coefficient can be estimated.

5. Conclusion

In this work, we presented an *in-situ*, computationally assisted experimental method for the determination of the effective ion-induced SEEC, γ, in a CCPs operated in argon gas. This method relies on the dependence of the DC self-bias voltage, η (that develops due to the EAE) on the SEEC in the case of dual-frequency excitation [30]. To this end, we designed and constructed a dedicated discharge cell called 'XS Cell', optimized operating conditions such as base frequencies, voltage amplitudes, and gas pressure to achieve the required experimental

accuracy and to operate the system under conditions where a relatively high sensitivity of η on γ is achieved. Therefore, relatively low operating frequencies of $f_1 = 2$ MHz and 4 MHz were chosen, and the pressure was set to 40 Pa and 80 Pa. These low frequency values were favored to avoid the electromagnetic resonance of the cell. In the experiments, voltage amplitudes $\phi_1 = 150$ V and $\phi_2 = 75$ V were selected for both base frequencies.

The simulations have been based on an extended PIC/MCC code coupled with a DRR code. The PIC/MCC code considered as 'targets' for electron-impact collisions of Ar atoms in different excited levels besides the ground-state atoms. The spatial distributions of the Ar atoms in these excited levels were computed by the DRR code based on the electron-impact collision rates computed in the PIC/MCC code. Through simulation, we varied the SEEC values to match with experimental results, thus determining the actual value of γ. Our findings, in agreement with typical literature data for argon and stainless steel electrodes approximate $\gamma \approx 0.07$. The understanding of the results has been aided by the analytical model of the EAE [64] that is based on a voltage balance of the RF discharge. We have shown that this model is able to successfully reproduce and explain the behavior of the DC self-bias voltage as a function of the γ.

This method represents a robust approach for determining γ in CCPs, exhibiting potential for precise *in-situ* measurement of this critical parameter. It should, however, be kept in mind that the accurate measurement of the RF voltage amplitudes is a strict requirement for this technique. If this is ensured, then our method provides an easier access to the effective SEEC as compared to other approaches, like γ-CAST, as implementation of phase-resolved optical emission spectroscopy could be impossible in practical plasma processing equipment. Future studies and laboratory experiments will further validate and expand upon this method, exploring different electrode materials and gases across various physical settings and discharge operating conditions keeping in mind that the method is restricted to conducting materials, as in the case of dielectric substances, which themselves act as capacitors, the measurement of the DC self-bias voltage is not well defined at any external point of contact.

Data availability statement

The data that support the findings of this study are available upon reasonable request from the authors.

Acknowledgments

Appendix

Table 4. Reduced set of electron-impact collision processes considered in the model. GS: ground state. Here, the Racah notation is used for the argon excited levels for compatibility with the notation in [40].

Process	Target		Product
1	GS	→	GS (elastic)
2	GS	→	Ar(4s[3/2]2)
3	GS	→	Ar(4s[3/2]1)
4	GS	→	Ar(4s'[1/2]0)
5	GS	→	Ar(4s'[1/2]1)
6	GS	→	Ar(4p[1/2]1)
7	GS	→	Ar(4p[5/2]3)
8	GS	→	Ar(4p[5/2]2)
9	GS	→	Ar(4p[3/2]1)
10	GS	→	Ar(4p[3/2]2)
11	GS	→	Ar(4p[1/2]0)
12	GS	→	Ar(4p'[3/2]1)
13	GS	→	Ar(4p'[3/2]2)
14	GS	→	Ar(4p'[1/2]1)
15	GS	→	Ar(4p'[1/2]0)
16	GS	→	Ar(3d[1/2]0)
17	GS	→	Ar(3d[1/2]1)
18	GS	→	Ar(3d[3/2]2)
19	GS	→	Ar(3d[7/2]4)
20	GS	→	Ar(5s[3/2]2)
21	GS	→	Ar(3d[7/2]3)
22	GS	→	Ar(5s[3/2]1)
23	GS	→	Ar(3d[5/2]2)
24	GS	→	Ar(3d[5/2]3)
25	GS	→	Ar(3d[3/2]1)
26	GS	→	Ar(5s'[1/2]0)
27	GS	→	Ar(5s'[1/2]1)
28	GS	→	Ar(3d'[5/2]2)
29	GS	→	Ar(3d'[3/2]2)
30	GS	→	Ar(3d'[5/2]3)
31	GS	→	Ar(3d'[3/2]1)
32	GS	→	Ar(Rydberg)
33	GS	→	$Ar^+ + e^-$
34	Ar(4s'[1/2]0)	→	Ar(4s'[1/2]1)
35	Ar(4s'[1/2]0)	→	Ar(4p[1/2]1)
36	Ar(4s'[1/2]0)	→	Ar(4p[3/2]1)
37	Ar(4s'[1/2]0)	→	Ar(4p'[3/2]1)
38	Ar(4s'[1/2]0)	→	Ar(4p'[1/2]1)
39	Ar(4s'[1/2]0)	→	Ar(5s'[1/2]0)
40	Ar(4s'[1/2]0)	→	Ar(3d'[5/2]2)
41	Ar(4s'[1/2]0)	→	Ar(3d'[3/2]2)
42	Ar(4s'[1/2]1)	→	Ar(4p[1/2]1)
43	Ar(4s'[1/2]1)	→	Ar(4p[5/2]3)
44	Ar(4s'[1/2]1)	→	Ar(4p[5/2]2)
45	Ar(4s'[1/2]1)	→	Ar(4p[3/2]1)
46	Ar(4s'[1/2]1)	→	Ar(4p[3/2]2)
47	Ar(4s'[1/2]1)	→	Ar(4p'[3/2]1)
48	Ar(4s'[1/2]1)	→	Ar(4p'[3/2]2)
49	Ar(4s'[1/2]1)	→	Ar(4p'[1/2]1)
50	Ar(4s'[1/2]1)	→	Ar(4p'[1/2]0)

(Continued.)

Table 4. (Continued.)

Process	Target		Product
51	Ar(4s'[1/2]1)	→	Ar(3d[5/2]3)
52	Ar(4s'[1/2]1)	→	Ar(5s'[1/2]1)
53	Ar(4s'[1/2]1)	→	Ar(3d'[5/2]2)
54	Ar(4s'[1/2]1)	→	Ar(3d'[3/2]2)
55	Ar(4s'[1/2]1)	→	Ar(3d'[5/2]3)
56	Ar(4s'[1/2]1)	→	Ar(3d'[3/2]1)
57	Ar(4s[3/2]1)	→	Ar(4s'[1/2]0)
58	Ar(4s[3/2]1)	→	Ar(4s'[1/2]1)
59	Ar(4s[3/2]1)	→	Ar(4p[1/2]1)
60	Ar(4s[3/2]1)	→	Ar(4p[5/2]3)
61	Ar(4s[3/2]1)	→	Ar(4p[5/2]2)
62	Ar(4s[3/2]1)	→	Ar(4p[3/2]1)
63	Ar(4s[3/2]1)	→	Ar(4p[3/2]2)
64	Ar(4s[3/2]1)	→	Ar(4p[1/2]0)
65	Ar(4s[3/2]1)	→	Ar(4p'[3/2]1)
66	Ar(4s[3/2]1)	→	Ar(4p'[3/2]2)
67	Ar(4s[3/2]1)	→	Ar(4p'[1/2]1)
68	Ar(4s[3/2]1)	→	Ar(3d[3/2]2)
69	Ar(4s[3/2]1)	→	Ar(5s[3/2]2)
70	Ar(4s[3/2]1)	→	Ar(3d[7/2]3)
71	Ar(4s[3/2]1)	→	Ar(5s[3/2]1)
72	Ar(4s[3/2]1)	→	Ar(3d[5/2]2)
73	Ar(4s[3/2]1)	→	Ar(3d[5/2]3)
74	Ar(4s[3/2]1)	→	Ar(3d[3/2]1)
75	Ar(4s[3/2]2)	→	Ar(4s[3/2]1)
76	Ar(4s[3/2]2)	→	Ar(4s'[1/2]0)
77	Ar(4s[3/2]2)	→	Ar(4s'[1/2]1)
78	Ar(4s[3/2]2)	→	Ar(4p[1/2]1)
79	Ar(4s[3/2]2)	→	Ar(4p[5/2]3)
80	Ar(4s[3/2]2)	→	Ar(4p[5/2]2)
81	Ar(4s[3/2]2)	→	Ar(4p[3/2]1)
82	Ar(4s[3/2]2)	→	Ar(4p[3/2]2)
83	Ar(4s[3/2]2)	→	Ar(4p[1/2]0)
84	Ar(4s[3/2]2)	→	Ar(4p'[3/2]1)
85	Ar(4s[3/2]2)	→	Ar(4p'[3/2]2)
86	Ar(4s[3/2]2)	→	Ar(4p'[1/2]1)
87	Ar(4s[3/2]2)	→	Ar(3d[1/2]0)
88	Ar(4s[3/2]2)	→	Ar(3d[1/2]1)
89	Ar(4s[3/2]2)	→	Ar(3d[3/2]2)
90	Ar(4s[3/2]2)	→	Ar(3d[7/2]4)
91	Ar(4s[3/2]2)	→	Ar(5s[3/2]2)
92	Ar(4s[3/2]2)	→	Ar(3d[7/2]3)
93	Ar(4s[3/2]2)	→	Ar(5s[3/2]1)
94	Ar(4s[3/2]2)	→	Ar(3d[5/2]2)
95	Ar(4s[3/2]2)	→	Ar(3d[5/2]3)
96	Ar(4s[3/2]2)	→	Ar(3d[3/2]1)
97	Ar(4s'[1/2]1)	→	Ar(4s'[1/2]0)
98	Ar(4s'[1/2]0)	→	Ar(4s[3/2]1)
99	Ar(4s'[1/2]1)	→	Ar(4s[3/2]1)
100	Ar(4s[3/2]1)	→	Ar(4s[3/2]2)
101	Ar(4s'[1/2]0)	→	Ar(4s[3/2]2)
102	Ar(4s'[1/2]1)	→	Ar(4s[3/2]2)
103	Ar(4s[3/2]2)	→	Ar$^+$ + e$^-$ (stepwise)
104	Ar(4s[3/2]1)	→	Ar$^+$ + e$^-$ (stepwise)
105	Ar(4s'[1/2]0)	→	Ar$^+$ + e$^-$ (stepwise)
106	Ar(4s'[1/2]1)	→	Ar$^+$ + e$^-$ (stepwise)

ORCID iDs

Ranna Masheyeva ⓘ https://orcid.org/0000-0002-6950-662X

Peter Hartmann ⓘ https://orcid.org/0000-0003-3572-1310

Karlygash Dzhumagulova ⓘ https://orcid.org/0000-0002-2937-4482

Yong-Xin Liu ⓘ https://orcid.org/0000-0002-6506-7148

Julian Schulze ⓘ https://orcid.org/0000-0001-7929-5734

Zoltán Donkó ⓘ https://orcid.org/0000-0003-1369-6150

References

[1] Makabe T and Petrović Z L 2014 *Plasma Electronics: Applications in Microelectronic Device Fabrication* vol 26 (CRC Press)

[2] Chabert P and Braithwaite N 2011 *Physics of Radio-Frequency Plasmas* (Cambridge University Press)

[3] Donnelly V M and Kornblit A 2013 *J. Vac. Sci. Technol.* A **31** 050825

[4] Heil B G, Czarnetzki U, Brinkmann R P and Mussenbrock T 2008 *J. Phys. D: Appl. Phys.* **41** 165202

[5] Kawamura E, Vahedi V, Lieberman M and Birdsall C 1999 *Plasma Sources Sci. Technol.* **8** R45

[6] Zhang Y, Zafar A, Coumou D J, Shannon S C and Kushner M J 2015 *J. Appl. Phys.* **117** 233302

[7] Krüger F, Wilczek S, Mussenbrock T and Schulze J 2019 *Plasma Sources Sci. Technol.* **28** 075017

[8] Bogdanova M, Lopaev D, Rakhimova T, Voloshin D, Zotovich A and Zyryanov S 2020 arXiv:2012.14882

[9] Phelps A and Petrovic Z L 1999 *Plasma Sources Sci. Technol.* **8** R21

[10] Derzsi A, Korolov I, Schüngel E, Donkó Z and Schulze J 2015 *Plasma Sources Sci. Technol.* **24** 034002

[11] Derzsi A, Horváth B, Donkó Z and Schulze J 2020 *Plasma Sources Sci. Technol.* **29** 074001

[12] Horváth B, Daksha M, Korolov I, Derzsi A and Schulze J 2017 *Plasma Sources Sci. Technol.* **26** 124001

[13] Horváth B, Schulze J, Donkó Z and Derzsi A 2018 *J. Phys. D: Appl. Phys.* **51** 355204

[14] Horváth B, Donkó Z, Schulze J and Derzsi A 2022 *Plasma Sources Sci. Technol.* **31** 045025

[15] Korolov I, Derzsi A, Donkó Z, Schüngel E and Schulze J 2016 *Plasma Sources Sci. Technol.* **25** 015024

[16] Sobolewski M A 2024 *Plasma Sources Sci. Technol.* **33** 085011

[17] Phelps A V 2001 *Plasma Sources Sci. Technol.* **10** 329

[18] Yamamura Y, Matsunami N and Itoh N 1983 *Radiat. Eff.* **71** 65–86

[19] Sydorenko D 2006 Particle-in-cell simulations of electron dynamics in low pressure discharges with magnetic fields *PhD Thesis* University of Saskatchewan

[20] Rauf S, Bera K and Collins K 2009 *Plasma Sources Sci. Technol.* **19** 015014

[21] Wen Y Y, Zhang Y R, Jiang G, Song Y H and Wang Y N 2019 *AIP Adv.* **9** 055019

[22] Mahdavipour B and Gudmundsson J 2024 *Plasma Sources Sci. Technol.* **33** 065006

[23] Donkó Z, Schulze J, Hartmann P, Korolov I, Czarnetzki U and Schüngel E 2010 *Appl. Phys. Lett.* **97** 081501

[24] Lafleur T, Chabert P and Booth J P 2013 *J. Phys. D: Appl. Phys.* **46** 135201

[25] Korolov I, Derzsi A, Donkó Z and Schulze J 2013 *Appl. Phys. Lett.* **103** 064102

[26] Daksha M, Berger B, Schuengel E, Korolov I, Derzsi A, Koepke M, Donkó Z and Schulze J 2016 *J. Phys. D: Appl. Phys.* **49** 234001

[27] Schulze J, Donko Z, Derzsi A, Korolov I and Schuengel E 2014 *Plasma Sources Sci. Technol.* **24** 015019

[28] Schulenberg D A, Korolov I, Donkó Z, Derzsi A and Schulze J 2021 *Plasma Sources Sci. Technol.* **30** 105003

[29] Schulze C, Donkó Z and Benedikt J 2022 *Plasma Sources Sci. Technol.* **31** 105017

[30] Masheyeva R, Dzhumagulova K, Myrzaly M, Schulze J and Donkó Z 2021 *AIP Adv.* **11** 075024

[31] Donkó Z, Schulze J, Heil B and Czarnetzki U 2008 *J. Phys. D: Appl. Phys.* **42** 025205

[32] Sobolewski M 1995 *IEEE Trans. Plasma Sci.* **23** 1006–22

[33] Press A F, Goeckner M J and Overzet L J 2019 *J. Vac. Sci. Technol.* B **37** 062926

[34] Horváth B, Derzsi A, Schulze J, Korolov I, Hartmann P and Donkó Z 2020 *Plasma Sources Sci. Technol.* **29** 055002

[35] Schulze J, Schüngel E, Donkó Z and Czarnetzki U 2011 *Plasma Sources Sci. Technol.* **20** 015017

[36] Korolov I, Donkó Z, Hübner G, Bischoff L, Hartmann P, Gans T, Liu Y, Mussenbrock T and Schulze J 2019 *Plasma Sources Sci. Technol.* **28** 094001

[37] Wen D Q, Krek J, Gudmundsson J T, Kawamura E, Lieberman M A and Verboncoeur J P 2021 *Plasma Sources Sci. Technol.* **30** 105009

[38] Wen D Q, Krek J, Gudmundsson J T, Kawamura E, Lieberman M A and Verboncoeur J P 2022 *IEEE Trans. Plasma Sci.* **50** 2548–57

[39] Donkó Z, Hartmann P, Korolov I, Schulenberg D, Rohr S, Rauf S and Schulze J 2023 *Plasma Sources Sci. Technol.* **32** 065002

[40] Zatsarinny O, Wang Y and Bartschat K 2014 *Phys. Rev.* A **89** 022706

[41] Baeva M, Bösel A, Ehlbeck J and Loffhagen D 2012 *Phy. Rev.* E **85** 056404

[42] BSR database (available at: www.lxcat.net/BSR) (Accessed 18 August 2022)

[43] Hyman H 1979 *Phys. Rev.* A **20** 855

[44] Lymberopoulos D P and Economou D J 1993 *J. Appl. Phys.* **73** 3668–79

[45] Phelps A V 1994 *J. Appl. Phys.* **76** 747–53

[46] Siepa S L 2017 Global collisional-radiative model for optical emission spectroscopy of argon and argon-containing plasmas *PhD Thesis Dissertation*, Bochum, Ruhr-Universität Bochum

[47] Tachibana K 1986 *Phys. Rev.* A **34** 1007

[48] Sadeghi N, Setser D, Francis A, Czarnetzki U and Döbele H 2001 *J. Chem. Phys.* **115** 3144–54

[49] Chang R and Setser D 1978 *J. Chem. Phys.* **69** 3885–97

[50] Ellis E and Twiddy N 1969 *J. Phys. B: At. Mol. Phys.* **2** 1366

[51] Chai K B and Kwon D H 2019 *J. Quant. Spectrosc. Radiat. Transfer* **227** 136–44

[52] Verboncoeur J P 2005 *Plasma Phys. Control. Fusion* **47** A231–60

[53] Lymberopoulos D P and Economou D J 1995 *J. Res. Natl Inst. Stand. Technol.* **100** 473

[54] Kim H, Iza F, Yang S, Radmilović-Radjenović M and Lee J 2005 *J. Phys. D: Appl. Phys.* **38** R283

[55] Donkó Z, Derzsi A, Vass M, Horváth B, Wilczek S, Hartmann B and Hartmann P 2021 *Plasma Sources Sci. Technol.* **30** 095017

[56] Pitchford L C *et al* 2017 *Plasma Process. Polym.* **14** 1600098

[57] Carbone E, Graef W, Hagelaar G, Boer D, Hopkins M M, Stephens J C, Yee B T, Pancheshnyi S, van Dijk J and Pitchford L 2021 *Atoms* **9** 16

[58] Gangwar R, Sharma L, Srivastava R and Stauffer A 2012 *J. Appl. Phys.* **111** 053307

[59] Donkó Z, Tsankov T V, Hartmann P, Arellano F J T, Czarnetzki U and Hamaguchi S 2024 *J. Phys. D: Appl. Phys.* **57** 375209

[60] Press W, Flannery B, Teukolsky S, Vetterling W and Chipperfield J 1987 *Numerical Recipes: The Art of Scientific Computing* (Cambridge University Press)

[61] Capriotti E R 1965 *Astrophys. J.* **142** 1101

[62] Bhatia A and Kastner S 2000 *J. Quant. Spectrosc. Radiat. Transfer* **67** 55–63

[63] Schulze J, Schüngel E, Donkó Z and Czarnetzki U 2010 *J. Phys. D: Appl. Phys.* **43** 225201

[64] Czarnetzki U, Heil B G, Schulze J, Donkó Z, Mussenbrock T and Brinkmann R P 2009 *J. Phys.: Conf. Ser.* **162** 012010